1-1-2019

Deformation and strength characteristics of Laves phases in titanium alloys

Chirag D. Rabadia
Edith Cowan University, c.rabadia@ecu.edu.au

Y. J. Liu

Liang-Yu Chen
Edith Cowan University, liangyu.chen@ecu.edu.au

Syed F. Jawed
Edith Cowan University, s.jawed@ecu.edu.au

L. Q. Wang

See next page for additional authors

10.1016/j.matdes.2019.107891
Rabadia, C. D., Liu, Y. J., Chen, L. Y., Jawed, S. F., Wang, L. Q., Sun, H., & Zhang, L. C. (2019). Deformation and strength characteristics of Laves phases in titanium alloys. *Materials & Design*, *179*, Article 107891. Available here

Materials and Design 179 (2019) 107891

Contents lists available at ScienceDirect

Materials and Design

journal homepage: www.elsevier.com/locate/matdes

Deformation and strength characteristics of Laves phases in titanium alloys

C.D. Rabadia [a], Y.J. Liu [b], L.Y. Chen [a,c], S.F. Jawed [a], L.Q. Wang [d,*], H. Sun [a], L.C. Zhang [a,*]

[a] School of Engineering, Edith Cowan University, 270 Joondalup Drive, Joondalup, Perth, WA 6027, Australia
[b] School of Engineering, The University of Western Australia, 35 Stirling Highway, Perth, WA 6009, Australia
[c] School of Science, Jiangsu University of Science and Technology, Zhenjiang, Jiangsu 212003, China
[d] State Key Laboratory of Metal Matrix Composites, School of Material Science and Engineering, Shanghai Jiao Tong University, Shanghai 200240, China

HIGHLIGHTS

- Indentation-based deformation is affected by the type of Laves phase present in the microstructure.
- The C15-type Laves phase deforms better than the C14-type Laves phase.
- The C15-type Laves phase could contribute in enhancing bulk plasticity of the alloy.
- The C14-type Laves phase exhibits a better dislocation-pinning ability than the C15-type Laves phase.

GRAPHICAL ABSTRACT

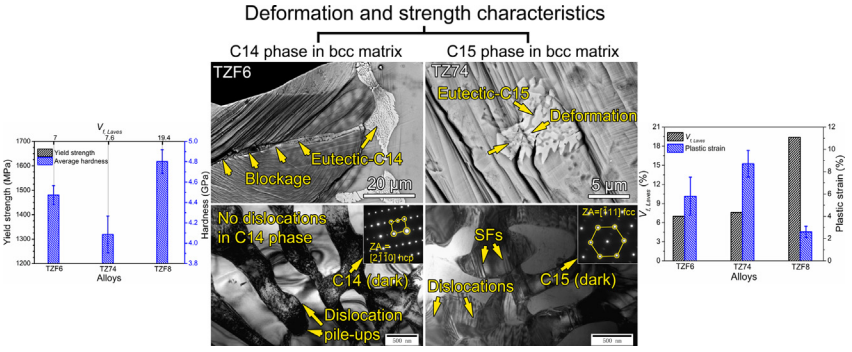

ARTICLE INFO

Article history:
Received 6 May 2019
Received in revised form 24 May 2019
Accepted 27 May 2019
Available online 28 May 2019

Keywords:
Titanium alloy
Micro-indentation
Laves phase
Deformation
Slip
Dislocation

ABSTRACT

The superior reinforcement nature of Laves phases make them suitable for high-strength applications. Therefore, investigations on the deformation and strength characteristics of Laves phases are useful in development of an improved Laves phase-reinforced alloy. In this work, the Vickers micro-indentation method is used to evaluate and compare the deformation and strength characteristics of a hexagonal close-packed Laves phase (C14-type) in Ti-35Zr-5Fe-6Mn (wt%) and a face-centered cubic Laves phase (C15-type) in Ti-33Zr-7Fe-4Cr (wt%), considering the same volume fraction of Laves phase (~7.0%) in these alloys. Moreover, the effects of higher volume fraction of Laves phase (19.4%) on indentation-based deformation features are evaluated in Ti-35Zr-5Fe-8Mn (wt%). Remarkably, dislocation activity and plastic deformation features are evident in the C15-type Laves phase, whereas the C14-type Laves phase strongly blocks dislocation motion. Therefore, the C15-type Laves phase improves plastic deformability, whereas the C14-type Laves phase improves strength characteristics of Laves phase-reinforced alloys.

1. Introduction

Laves phases have become a promising strengthening agent in alloys suitable for automotive, aerospace and petrochemical applications, where Laves phase-reinforced alloys exhibit high strength along with

* Corresponding authors.
E-mail addresses: wang_liqiang@sjtu.edu.cn (L.Q. Wang), l.zhang@ecu.edu.au (L.C. Zhang).

https://doi.org/10.1016/j.matdes.2019.107891

superior hardness [1–3]. Hence, research interests have been increasingly investigating the deformation and strength characteristics of Laves phases, which may be favorable to develop an improved Laves phase-reinforced alloy for several structural applications. Usually, the following three types of Laves phases are formed with AB_2 compositions of various elements: (i) C14, (ii) C15 and (iii) C36 [4]. The prototype structures of C14-type, C15-type and C36-type Laves phases are $MgZn_2$, $MgCu_2$ and $MgNi_2$ respectively [5]. Among these three types of Laves phases, C14-type and C15-type phases are formed frequently, whereas the C36-type phase is rarely formed [6]. The formation of Laves phases primarily depends on a geometric parameter, i.e., atomic radii ratio of A and B atoms (where A has a relatively larger atomic size and B has a relatively smaller atomic size), the electronegativity difference between A and B atoms and the valence electron concentration [7–9]. Other than these, the transformation of Laves phase from other phases is also possible when an alloy undergoes a thermal processing and/or mechanical deformation [10,11]. Furthermore, C14-type phases possess a hexagonal close-packed (hcp) structure [12], whereas C15-type phases have a face-centered cubic (fcc) structure [1]. Therefore, the deformation and strengthening behavior of C14-type and C15-type Laves phases towards the dislocation activities should be different from each other due to different crystal structures.

It is well-known that indentation methods are non-destructive, less time consuming, more simplistic and inexpensive compared to conventional mechanical testing methods and they can effectively elucidate the deformation characteristics of a material [13]. The formation of crack and/or deformation bands occurs around and beneath the impression of hardness indentation [14,15]. Based on these features, deformation behavior and other mechanical properties such as hardness, elastic modulus, strain-hardening exponent, yield strength and fracture toughness can be estimated using indentation methods [16,17], where these properties are correlated directly with the microstructure of a material [18]. Considering these advantages, the Vickers micro-indentation method was chosen in this work to investigate the deformation features of the investigated alloys.

It has been reported that a C14-type Laves phase forms in Ti-Zr-Fe-Mn alloys [19] and a C15-type Laves phase precipitates in Ti-Zr-Fe-Cr alloys [1]. The values of atomic radii ratio for both the Ti-Zr-Fe-Mn and Ti-Zr-Fe-Cr systems are >1.200, which is very close to the ideal value of atomic radii ratio (1.225) for forming the Laves phase [1,19]. Therefore, Laves phases precipitate in the investigated Ti-Zr-Fe-Mn and Ti-Zr-Fe-Cr alloy systems when the alloys are rapidly cooled. On the other hand, Strukturbericht designation (C14/C15/C36) and volume fraction of the Laves phase ($V_{f,\ Laves}$) depend on the alloying elements and their quantities [8,20]. Hence, the quantities of alloying elements in the two aforementioned systems of alloys are selected in such a manner that the C15 phase is formed in the Ti-Zr-Fe-Cr alloys and the C14 phase is precipitated in the Ti-Zr-Fe-Mn alloys according to their respective phase diagrams and the findings in the previous literature [1,19–25]. Moreover, apart from the mechanical characterizations of the Ti-Zr-Fe-Mn alloys containing a C14 phase and the Ti-Zr-Fe-Cr alloys containing a C15 phase, the deformation and strength characteristics of C14 and C15 type phases in the two aforementioned quaternary alloy systems can also be a great area of research in the development of improved high-strength alloys.

Hence, considering the points discussed above, two C14-type alloys, i.e., Ti-35Zr-5Fe-6Mn (wt%) (abbreviated as TZF6) and Ti-35Zr-5Fe-8Mn (wt%) (abbreviated as TZF8) [19], and one C15-type alloy, i.e., Ti-33Zr-7Fe-4Cr (wt%) (abbreviated as TZ74) [1] were selected in this work. The primary aim of selecting the TZF6 and TZ74 alloys was to compare the indentation-based deformation and dislocation-pinning behavior of C14-type and C15-type Laves phases in the body-centered cubic (bcc) β- titanium (Ti) matrix because TZF6 (7.0 ± 0.5%) [19] and TZ74 (7.6 ± 0.7%) [1] comprise nearly identical $V_{f,\ Laves}$. On the other hand, $V_{f,\ Laves}$ for TZF8 is 19.4 ± 0.4% [19], which is greater than other two selected alloys (i.e., TZF6 and TZ74). Thus, the present work also investigates the effects of higher $V_{f,\ Laves}$ (19.4 ± 0.4%) on the deformation characteristics of TZF8. In addition, Ti alloys comprising a β phase were selected in this work because β-Ti alloys can be used in many structural and biomedical applications [26,27] as β-Ti alloys possess a low density and exhibit a superior balance of strength and ductility as well as excellent corrosion resistance [28–30]. The β phase in Ti alloys comprises a bcc structure which is also effective in improving bulk plasticity of Laves phase-reinforced alloys [2,9]. The advantage of the bcc matrix is that it possesses a total of 48 slip systems and exhibits high dislocation density after deformation in multi-phase alloys due to the dislocation-pinning produced by second phase precipitates/particles [28,31,32]. Second phase precipitates/particles produce a stress field, which hinders the dislocation motion to pass through them due to comprising different atomic sequence and/or different crystal structure. This phenomenon is known as dislocation-pinning. In the present work, dislocation-pinning could be produced by the precipitated Laves phases (C14 and C15) at the Laves (C14/C15)-β interfaces, which usually leads to an improved strengthening effect in an alloy. Consequently, dislocation activities at Laves (C14/C15)-β interfaces and in the interior of Laves (C14/C15) phases are investigated with aim to shed insight into: (i) the deformability of C14 type and C15 type Laves phases, (ii) the occurrence of dislocation-pinning and (iii) the precipitation strengthening due to the presence of respective Laves phase (C14/C15). These findings are useful in optimizing strength and plasticity in emerging Laves phase-reinforced alloys.

2. Experimental procedure

TZF6, TZ74 and TZF8 were first cast from the alloying elements with a purity of 99.9% using a cold crucible levitation melting furnace and then rapidly quenched in a water-cooled copper crucible. Multiple cylindrical rods (4.6 mm diameter) of each alloy were produced from the respective cast ingot using wire electrical discharge machining. Eight Vickers micro-hardness indentations were performed at room temperature on multiple samples of each alloy using a Zwick Roell ZHU at: 5 kgf (49.03 N), 10 kgf (98.06 N) and 30 kgf (294.19 N) and at a dwelling time of 20 s. The bonding-interface technique was used to study the subsurface deformation features [14,33]. Scanning electron microscopy (SEM) was performed using a FEI Verios XHR 460 microscope. Transmission electron microscopy (TEM), selected area electron diffraction (SAED) and energy dispersive X-ray spectroscopy (EDX) were performed using a JEOL JEM-2100 microscope. The samples of each alloy for SEM were ground using SiC papers up to 2000 grits and then polished using a Struers MD-Chem polishing cloth with a presence of Struers OP-S colloidal silica, according to standard metallographic procedures. Specimens for TEM were prepared from the 3 mm discs by electropolishing in a mixture of ethanol and perchloric acid with a proportion of 9:1 by volume at a temperature of −30 °C with an electrode voltage of 30–90 V [34]. Microstructure, indentation-based deformation and strength characteristics of Laves phases were analyzed using SEM, TEM, EDX and SAED patterns. ImageJ software was used for all the types of length measurements discussed in this work. The reported values of $V_{f,\ Laves}$ were estimated using ImageJ software (threshold function) from the low-magnification backscattered SEM images of all the investigated alloys.

3. Results and discussion

Table 1 summarizes the information of phase constituents (including Strukturbericht designation and chemical formula of Laves phases), $V_{f,\ Laves}$, V_{β}, lattice parameters, grain size, lamellar spacing, yield strength and plastic strain for the investigated alloys, as reported in Ref. [1, 19]. The values of these properties are used to carry out further discussion related to deformation characteristics of the investigated alloys in this work. The inverse correlation between yield strength and grain size for the TZF6, TZ74 and TZF8 alloys can be seen in Table 1. The reason

Table 1
The summary of phase constituents, $V_{f,\ Laves}$ (volume fraction of Laves phase), $V_{f,\beta}$ (volume fraction of β phase), lattice parameters (α), grain size, lamellar spacing, yield strength and plastic strain for the TZF6 (Ti-35Zr-5Fe-6Mn), TZ74 (Ti-33Zr-7Fe-4Cr) and TZF8 (Ti-35Zr-5Fe-8Mn) alloys.

Alloys	Phase constituents	$V_{f,\ Laves}$ (%)	$V_{f,\beta}$ (%)	α_{Laves} (nm)	α_{β} (nm)	Grain size (μm)	Lamellar spacing (nm)	Yield strength (MPa)	Plastic strain (%)	Ref.
TZF6	β, C14-Zr(Fe, Mn)$_2$	7.0 ± 0.5	93.0 ± 0.5	a = 0.5198, c = 0.8515	a = 0.3320	49 ± 18	877 ± 291	1485 ± 18	5.8 ± 1.7	[19]
TZ74	β, C15-Zr(Fe, Cr)$_2$	7.6 ± 0.7	92.4 ± 0.7	a = 0.7069	a = 0.3351	63 ± 23	396 ± 137	1285 ± 42	8.7 ± 1.2	[1]
TZF8	β, C14-Zr(Fe, Mn)$_2$	19.4 ± 0.4	80.6 ± 0.4	a = 0.5197, c = 0.8505	a = 0.3311	18 ± 7	1091 ± 508	1580 ± 24	2.6 ± 0.5	[19]

for such an inverse correlation in the investigated alloys is grain boundary strengthening which occurs according to the Hall-Petch relationship [35–38]. The values of lamellar spacing (inside the Laves phase morphologies) are inversely correlated with the values of plastic strain presented in Table 1 for all the investigated alloys. On the other hand, $V_{f,\ Laves}$ of TZF6 and TZ74 are almost identical (Table 1). Therefore, it is quite motivating, based on the results presented in Table 1, to further investigate and compare the deformation and dislocation-pining behavior of the C14-type phase in TZF6 and the C15-type phase in TZ74.

Figs. 1–3 illustrate the SEM images of hardness indentations obtained at 294.19 N for the investigated alloys. Figs. 1b, 2b and 3b display the precipitated eutectic morphologies (white) of C14 and C15 phases over the β matrix [1,19]. Inside the eutectic morphologies of Laves phase (C14/C15), the white regions are the regions of the Laves phase,

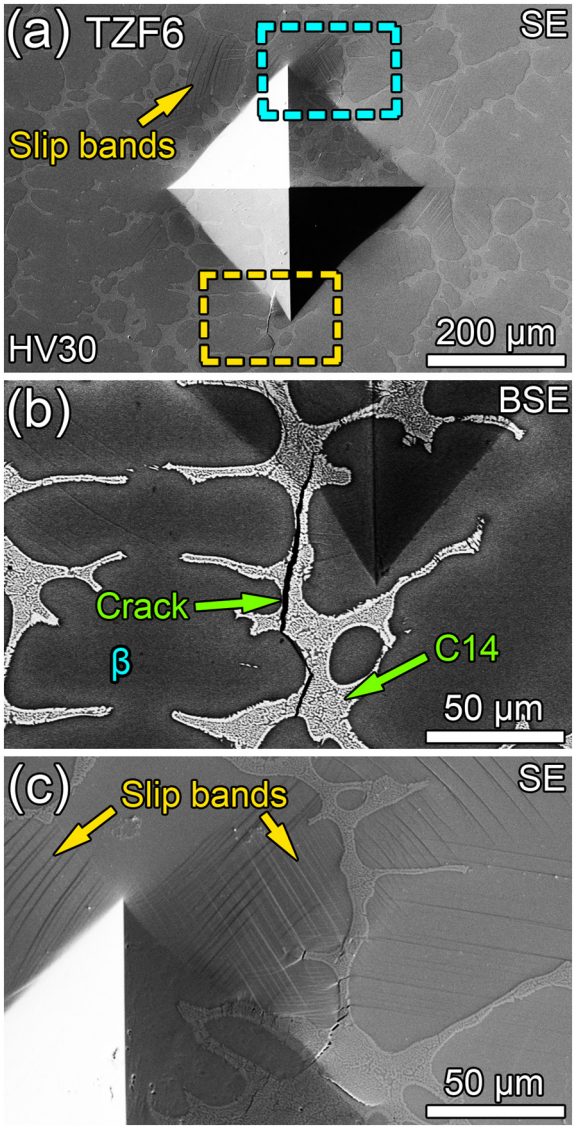

Fig. 1. The SEM images of micro-hardness indentation taken for TZF6 (Ti-35Zr-5Fe-6Mn) at 294.19 N (HV30). Note that secondary electron mode and back-scattered electron mode are labelled as SE and BSE respectively in (a)–(c). (b) and (c) are the high-magnification images of the area selected using yellow and sky-blue rectangles shown in (a) respectively.

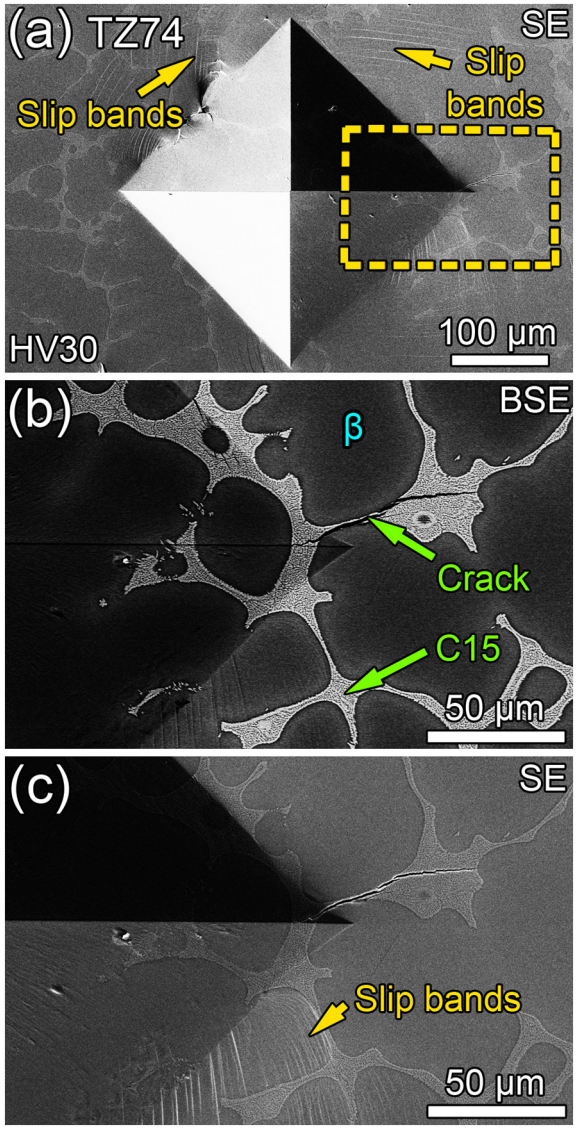

Fig. 2. The SEM images of micro-hardness indentation taken for TZ74 (Ti-33Zr-7Fe-4Cr) at 294.19 N (HV30). Note that secondary electron mode and back-scattered electron mode are labelled as SE and BSE respectively in (a)–(c). (b) and (c) are the high-magnification images captured in BSE and SE modes respectively over the area selected using yellow rectangle shown in (a).

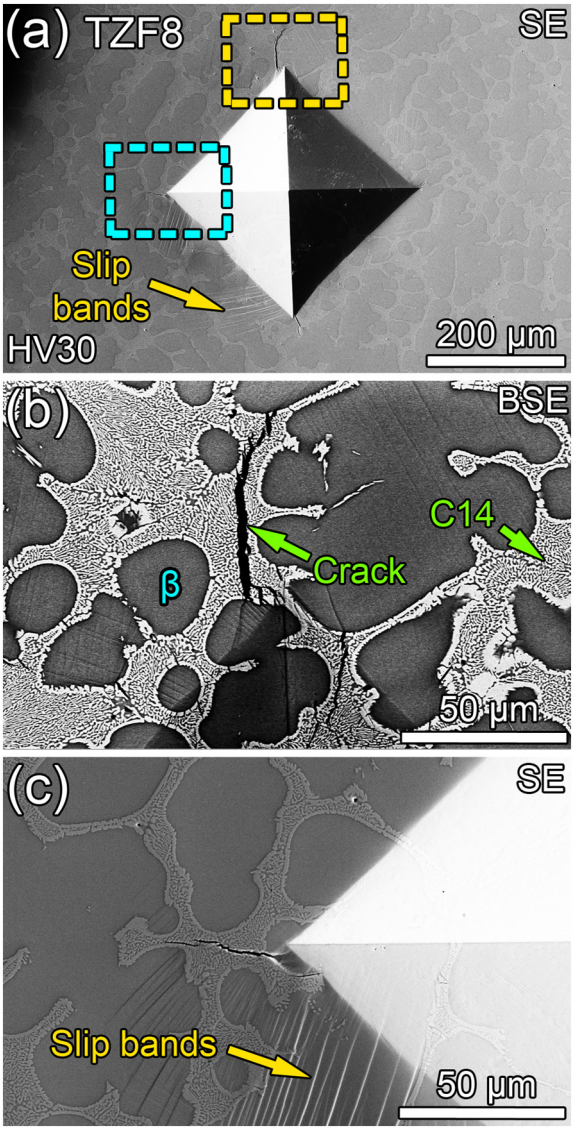

Fig. 3. The SEM images of micro-hardness indentation taken for TZF8 (Ti-35Zr-5Fe-8Mn) at 294.19 N (HV30). Note that secondary electron mode and back-scattered electron mode are labelled as SE and BSE respectively in (a)–(c). (b) and (c) are the high-magnification images of the area selected using yellow and sky-blue rectangles shown in (a) respectively.

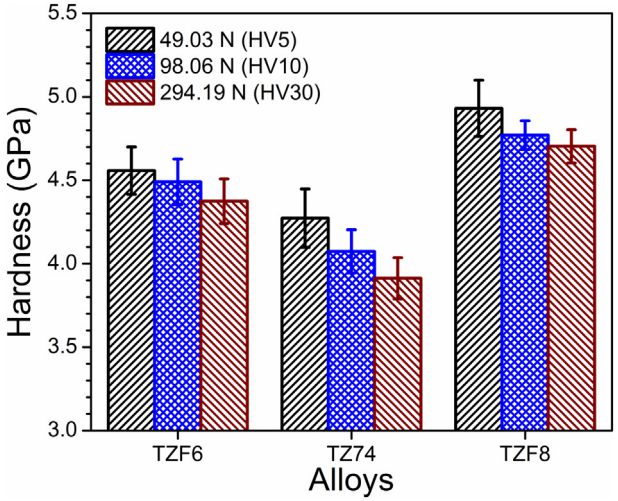

Fig. 4. Hardness of the TZF6 (Ti-35Zr-5Fe-6Mn), TZ74 (Ti-33Zr-7Fe-4Cr) and TZF8 (Ti-35Zr-5Fe-8Mn) alloys.

while the dark grey regions are with the β phase. Note that the regions of β phase (dark grey) present inside the eutectic morphologies of C14- and C15-type Laves phases (shown in Figs. 1–3) are not considered while estimating $V_{f,\ Laves}$ (as presented in Table 1). The crystal structures of C14 and C15 phases are confirmed using SAED patterns and discussed in succeeding explanations. EDX elemental compositions were measured on the C14 phase in TZF6 and the C15 phase in TZ74 [39–42], i.e., Ti-48.5Zr-13.8Fe-11.9Mn (wt%) and Ti-47.8Zr-182.Fe-8.9Cr (wt%), respectively. This indicates that the C14 and C15 precipitates are mainly composed of (Zr, Fe and Mn) and (Zr, Fe and Cr), respectively. Consequently, the AB_2 phase compositions of the C14 (in TZF6 and TZF8) and C15 (in TZ74) phases are $Zr(Fe, Mn)_2$ and $Zr(Fe, Cr)_2$ respectively (Table 1). On the other hand, the compositions of the β phase are closer to their nominal compositions.

The indentation size effect (ISE) in the present work features for the investigated alloys as hardness of the as-cast alloys decreases as the indentation-load increases from 49.03 N to 294.19 N (Fig. 4) [43]. ISE generally depends on the geometrically required dislocations, surface morphology, tip defects, creep and so on [44,45]. Established literature acknowledges that ISE vanishes at critical load and the values of hardness do not decrease further after critical load [46]. However, in the present work, this phenomenon (vanishing of ISE at certain load) is not observed in hardness testing performed until 294.19 N as the decreasing trend of hardness continues in hardness testing performed until 294.19 N (from 49.03 N) for the investigated alloys. The crack/deformation features formed around the indentations of TZF6 can be compared with those of TZ74 in Figs. 1 and 2, while the effect of high $V_{f,\ Laves}$ on crack/deformation patterns of TZF8 can be seen in the form of cracks in the SEM images shown in Fig. 3, as evidenced by the large cracks at the indentation-vertices of TZF8 when compared to TZ74 and TZF8. Although cracks at the indentation vertices are a common feature for brittle materials, the formation of cracks around the indentation depends on the underlying microstructure [18]. In case of two-phase alloys in which one phase is very brittle and the other is soft, there is a little possibility of the crack-formation at indentation-vertices if indentation vertices are located on a soft phase [18,19,47]. This phenomenon can be supported in the indentation images of the as-cast alloys as cracks deflect along the brittle C14 and C15 type Laves phases (Figs. 1–3). This clearly indicates that the β phase absorbs more fracture energy than Laves phases and dissipates the absorbed fracture energy to plastic deformation.

Other than cracks, slip bands are formed (because of dislocation motion) around indentations of the investigated alloys [48,49]. Table 2 presents the measured size of deformation zone around the indentations (δ) (at 98.06 N and 294.19 N) for the investigated alloys. The values of δ evidently increase as the load increases from 98.06 N to 294.19 N. In those indentations taken at 98.06 N and 294.19 N, the highest values of δ are obtained in TZ74, followed by TZF6 and TZF8 (Table 2), which indicates that the C15-type TZ74 alloy has better plastic deformability

Table 2
The values of measured δ (size of deformation zone around the indentations) and theoretical size of deformation zone δ_K obtained at indentation-loads (P) of 98.06 N and 294.19 N for the TZF6 (Ti-35Zr-5Fe-6Mn), TZ74 (Ti-33Zr-7Fe-4Cr) and TZF8 (Ti-35Zr-5Fe-8Mn) alloys.

Alloys	P (N)	Measured δ (μm)	Theoretical δ_K (μm)
TZF6	98.06	164 ± 4	177
	294.19	255 ± 7	307
TZ74	98.06	182 ± 2	191
	294.19	267 ± 5	330
TZF8	98.06	155 ± 6	172
	294.19	247 ± 12	298

than the C14-type TZF6 and TZF8 alloys. According to the continuum model suggested by Kramer et al. [50], the theoretical size of deformation zone (δ_K) around the indentation can be calculated by Eq. (1):

$$\delta_K = \left[\frac{3P}{(2\pi\sigma_{0.2})}\right]^{0.5} \quad (1)$$

where P is indentation-load and $\sigma_{0.2}$ is yield strength. As such, the theoretical values of δ_K were calculated for the investigated alloys at 98.06 N and 294.19 N. It is interesting to note that these δ_K values are close to those of the measured δ (Table 2) at 98.06 N but not at 294.19 N. This means that the Kramer's continuum model is valid in predicting δ up to a certain load limit. Moreover, the size of the indent remains smaller for the indents taken at 49.03 N compared with the sizes of the indents taken at 98.06 N and at 294.19 N. Therefore, in hardness testing, the indents taken at 98.06 N and 294.19 N cover a larger region of the microstructure comprising β phase and Laves (C14/C15) phase morphologies in the investigated alloys than those taken at 49.03 N. Therefore, the deformation features obtained at 49.03 N have not been used in this work.

Figs. 5 and 6 show the back-scattered SEM images of subsurface morphologies obtained at 98.06 N for the TZF6 and TZ74 alloys respectively. In TZF6 and TZ74, two types of deformation-induced slip steps are found: (i) primary (semi-circular) slip steps and (ii) secondary (radial) slip steps which usually propagate along the top indentation surface or from indenter tip [14]. Radial slip steps are shown in Figs. 5b and 6a and are indicated by small yellow arrows in Fig. 6b. The semi-circular and radial slip steps are formed because of the radial and shear stress components respectively and moreover, radial slip steps are usually formed after the semi-circular slip steps [33]. As the indentation performed for TZF6 at 98.06 N was around 10° inclined from the bonded interface, the epicentres of semi-circular slip steps are orientated towards left from the indenter tip. However, it is noteworthy to see that the C14 phase blocks the propagation of slip steps. As a result, accumulation of slip steps occurs just above the C14 phase, which can be clearly seen in Figs. 5a and 5c. Consequently, the C14 phase becomes a high-stress concentrated region which leads to the crack formation along the C14 phase (as indicated by white arrows in Fig. 5a). Further, new sets of semi-circular slip steps and radial slip steps are also formed below the C14 phase where the fracture line is shown by white arrows.

By contrast, the blockage behavior of C15 phase is not observed in TZ74 as the propagation direction of slip steps is barely disturbed below the C15 phase (Figs. 6b and 6c). In fact, slip steps propagate along the C15 phase in Fig. 6c (as indicated by yellow arrows). This shows that slip steps can propagate through the C15 phase but cannot do so through the C14 phase because the respective crystal structure of each phase may influence the dislocation activity and therefore the propagation of slip steps.

Furthermore, fewer slip steps are found in subsurface morphologies obtained at 98.06 N and 294.19 N for TZF8 (Fig. 7) compared to TZF6 and TZ74. A large crack is also found at 294.19 N in TZF8 (Fig. 7d), which indicates that TZF8 is more brittle compared to TZF6 and TZ74. In addition, spacing between slip steps (S) in subsurface morphologies obtained at 294.19 N was measured from the indenter tip in the four different zones as depicted in Table 3. It is evident that S increases as the distance of slip steps increases from the indenter tip [14,51]. This means that slip steps remain closely spaced near the indenter tip and widely spaced as the distance of slip steps increases from the indenter tip. A lower value of S indicates the occurrence of large plastic deformation, while a higher value of S suggests less plastic deformation in the respective zones [14]. Table 3 demonstrates that S for TZ74 is the lowest in all four zones followed by TZF6 and the highest in TZF8. The values of S reveal that TZ74 has a better plastic deformability than TZF6 and TZF8.

Table 3 summarizes the measured size of the subsurface deformation zone (λ) for the investigated alloys at 98.06 N and 294.19 N. Giannakopoulos and Suresh [16] have suggested that λ can be estimated by Eq. (2):

$$\lambda = \frac{0.3P}{{\sigma_{0.2}}^c} \quad (2)$$

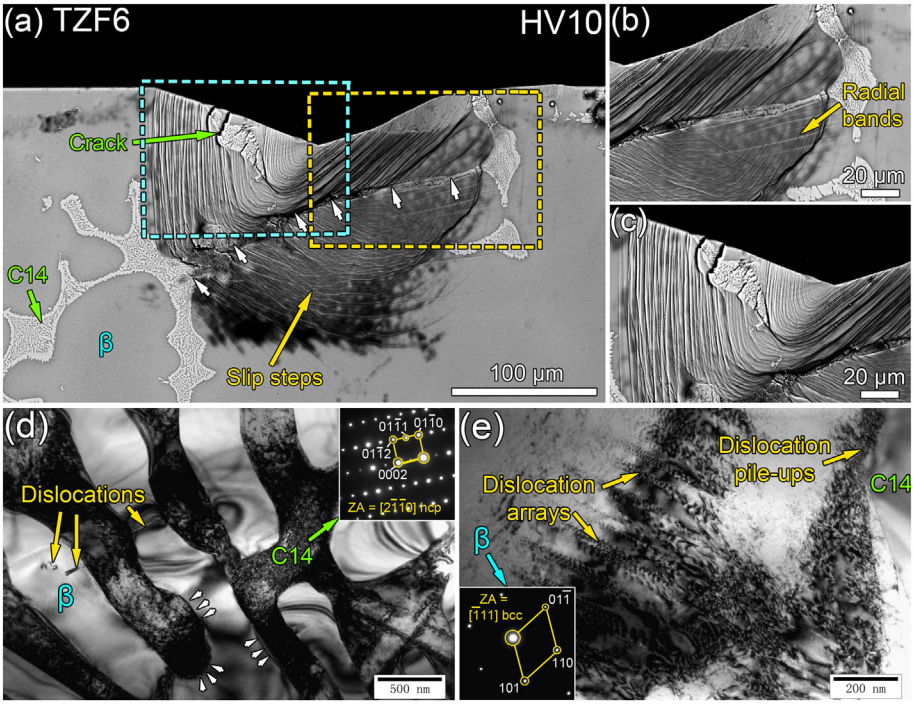

Fig. 5. The backscattered SEM images of the subsurface deformation morphologies formed at 98.06 N (HV10) for TZF6 (Ti-35Zr-5Fe-6Mn). (b) and (c) are the high-magnification images of the area selected using yellow and sky-blue rectangles respectively in (a). The bright field TEM images of (d) eutectic C14 phase and (e) the area outside the C14 phase at the C14-β phase interface of TZF6. The inset images in (d) and (e) are the SAED patterns of C14 (hcp) and β (bcc) phases respectively.

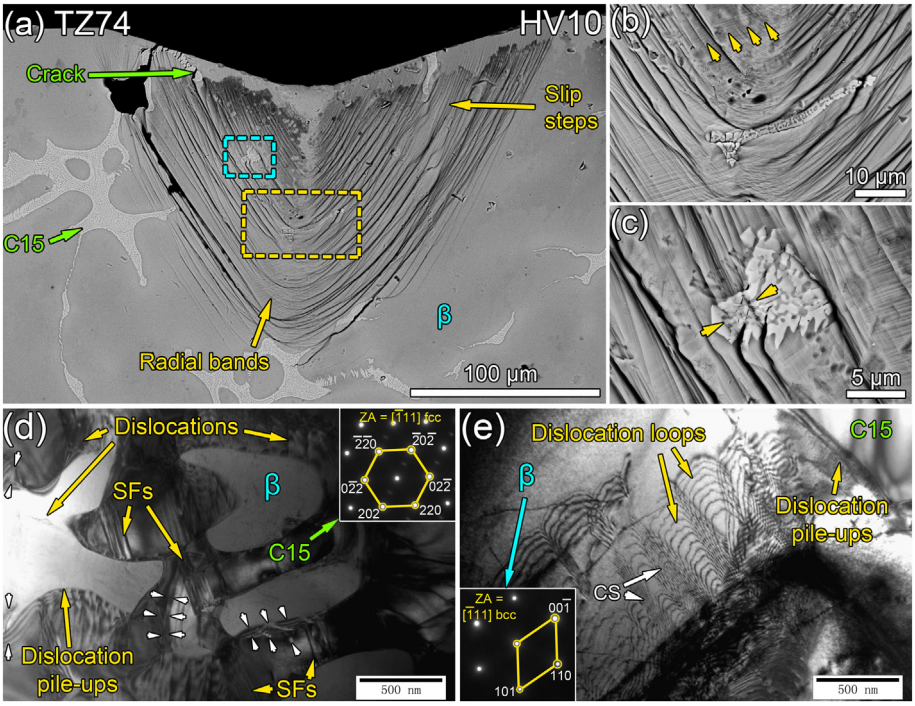

Fig. 6. The backscattered SEM images of the subsurface deformation morphologies formed at 98.06 N (HV10) for TZ74 (Ti-33Zr-7Fe-4Cr). (b) and (c) are the high-magnification images of the area selected using yellow and sky-blue rectangles respectively in (a). The bright field TEM images of (d) eutectic C15 phase and (e) the area outside the C15 phase at the C15-β phase interface of TZ74. The inset images in (d) and (e) are the SAED patterns of C15 (fcc) and β (bcc) phases respectively. Stacking faults and cross slips are labelled as SFs and CS respectively.

where P is indentation load and $\sigma^{c}_{0.2}$ is yield strength in compression. Based on Eq. (2), λ for all the as-cast alloys was calculated at 98.06 N and 294.19 N and the corresponding results are summarized in Table 3. For the investigated alloys, there is a little difference between the measured and calculated values of λ obtained at 98.06 N; nonetheless, there is a significant difference between the measured and

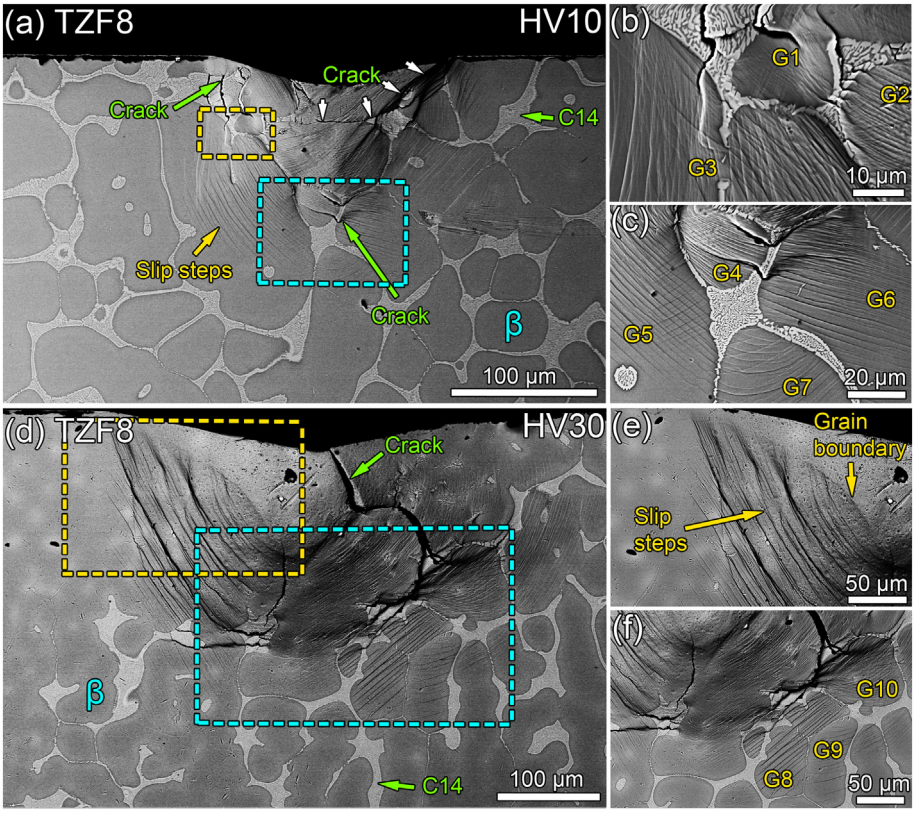

Fig. 7. The backscattered SEM images of the subsurface deformation morphologies formed at (a) 98.06 N (HV10) and (d) 294.19 N (HV30) for TZF8 (Ti-35Zr-5Fe-8Mn). (b) and (c) are the high-magnification images of the area selected using yellow and sky-blue rectangles respectively in (a). (e) and (f) are the high-magnification images of the area selected using yellow and sky-blue rectangles respectively in (d).

Table 3
The values of *S* (spacing between slip steps) measured at 294.19 N and the measured and calculated values of λ (size of the subsurface deformation zone) at 98.06 N and 294.19 N for TZF6 (Ti-35Zr-5Fe-6Mn), TZ74 (Ti-33Zr-7Fe-4Cr) and TZF8 (Ti-35Zr-5Fe-8Mn).

Alloys	*S* measured from the indenter-tip at 294.19 N load in subsurface morphologies, μm				λ at 98.06 N load, μm		λ at 294.19 N load, μm	
	<50 μm	50–100 μm	100–200 μm	>200 μm	Measured	Calculated	Measured	Calculated
TZF6	0.68 ± 0.22	0.73 ± 0.27	2.03 ± 0.52	2.62 ± 0.76	152	141	270	244
TZ74	0.59 ± 0.14	0.70 ± 0.13	1.10 ± 0.55	2.65 ± 0.47	158	151	351	262
TZF8	–	2.07 ± 0.64	2.64 ± 1.45	5.02 ± 1.97	141	136	279	236

calculated values of λ obtained at 294.19 N. This indicates that the Giannakopoulos-equation is also valid for calculating λ up to a certain load limit. Other than this, the measured and calculated values of λ at 98.06 N and 294.19 N for TZ74 are greater than the corresponding ones of TZF6 and TZF8. The values of λ and *S* indicate better plastic deformability in TZ74 than in TZF6 and TZF8.

A change in the direction of dislocation motion occurs when dislocations pass through grain boundaries or through the second phase precipitated on grain boundaries, because each grain has different crystal orientation [52–55]. Therefore, the dislocation activities in each grain remain different depending on the number of active slip systems and crystallographic orientation [54]. This phenomenon can be observed in grains G1-G10 shown in Fig. 7 as multiple types/sets of slip steps in individual grains in different directions are formed in grains G1–G10.

The TEM images were taken over the deformed C14 (Fig. 5d) and C15 phases (Fig. 6d) as well as over the C14-β (Fig. 5e) and C15-β interfaces (Fig. 6e). The C14, C15 and β phases are shown in Figs. 5 and 6. The morphologies of C14 and C15 eutectic phases look similar; however, their crystal structures remain different [56,57]. This can be confirmed by SAED patterns of C14 and C15 presented in Figs. 5d and 6d which reveal the hcp structure of C14 at a zone axis (ZA) of $[2\bar{1}\bar{1}0]$ and the fcc structure of C15 at a ZA of $[\bar{1}11]$. On the other hand, Figs. 5e and 6e reveal the bcc structure of β phase at a ZA of $[\bar{1}11]$ in the respective investigated alloys.

In Fig. 5d, dislocation activities in the C14 phase (dark) is not observed, while dislocations are evident in the β-bcc matrix. Dislocation pile-ups are also shown in Fig. 5d using white arrows. Moreover, immense dislocation density can be seen in Fig. 5e which was captured outside the C14 phase at the C14-β interface. In Fig. 5e, parallel arrays of dislocations are found, which look like screw dislocations. Additionally, dislocation tangles at many places are also evident in the β region (Fig. 5e). Further, intensive dislocation pile-ups at the C14-β interface can also be clearly seen. Figs. 5d and 5e reveal dislocation-less features in the C14 phase and its strong blockage behavior to dislocation motion because a hcp structure comprises only 3 slip systems and it is not intended to deform much, which makes this phase a high-stress concentration region and causes failure of the phase without showing much plastic deformation [58].

By contrast, in Fig. 6d, several dislocations and stacking faults (SFs) are found in the C15 phase (dark). SFs shown in Fig. 6d are probably formed on the same plane. SFs are planer defects in which the regular stacking sequence is disturbed and SFs usually play a significant role in improving plasticity of crystals along with dislocations [58]. Moreover, dislocation pile-ups also occur at the C15 phase boundary (Fig. 6d). Interestingly, transfer of slips from bcc to fcc at C15-β interfaces are also found at many places in Fig. 6d (white arrows), which improves bulk plasticity [59]. Therefore, TZ74 exhibits better plasticity than TZF6. Less dislocations are also observed in the β phase present inside the C15 phase; however, such a low dislocation number is still greater than those found in the β phase present inside the C14 phase. In Fig. 6e, gliding of dislocations form many dislocation loops. Dislocation loops also intersect with other loops, which is known as cross slips that do not disturb the dislocation motion of other loops. Furthermore, although dislocation pile-ups are also seen at the C15 phase boundary in Fig. 6e; however, the pile-ups are not as intense as observed in Fig. 5e. Figs. 6d and 6e reveal that the C15 phase has better deformability than the C14 phase because a fcc structure comprises more slip systems (12 in total) than a hcp structure (3 in total). Consequently, intensive dislocation pile-ups occur at the phase boundary of the C14 phase than that of the C15 phase. Hence, TZF6 exhibits higher yield strength and hardness, while it demonstrates lower plastic strain than TZ74 even though both comprise the same $V_{f,\ Laves}$ (Table 1). On the other hand, plastic deformation is evident in the C15 phase (Fig. 6c). This means that more than five slip systems should be active in the C15 phase according to the Von-Mises criterion [58].

4. Conclusions

The following are the main concluding remarks of the present work.

- The indentation-based deformation characteristics of the C14-type Laves phase in Ti-35Zr-5Fe-6Mn and the C15-type Laves phase in Ti-33Zr-7Fe-4Cr are carried out and compared with each other.
- The results in this work demonstrate that the type of Laves phase (C14/C15) and the volume fraction of Laves phase influence the indentation-based deformation characteristics.
- Although dislocation pile-ups occur at the phase boundaries of both C14 and C15 phases, the C14-type Laves phase immensely hinders the dislocation motion compared to the C15-type Laves phase. Therefore, the precipitation strengthening (dislocation pinning) ability of the C14 phase is better than the C15 phase.
- The dislocation activities and plastic deformation in the C15 phase are evident and are useful in obtaining an improved bulk-plasticity.

CRediT authorship contribution statement

C.D. Rabadia: Conceptualization, Methodology, Investigation, Writing - original draft, Writing - review & editing. **Y.J. Liu:** Investigation, Writing - review & editing. **L.Y. Chen:** Investigation, Writing - review & editing. **S.F. Jawed:** Investigation. **L.Q. Wang:** Investigation. **H. Sun:** Writing - review & editing. **L.C. Zhang:** Conceptualization, Methodology, Investigation, Writing - original draft, Writing - review & editing, Supervision.

Acknowledgement

The authors would like to acknowledge the financial support provided by National Natural Science Foundation of China under Grant No. 51674167. C.D. Rabadia and S.F. Jawed are grateful for the financial support from the ECU Postgraduate Research Scholarship and ECU - HEC Joint Scholarship respectively.

Data availability statement

The raw/processed data required to reproduce these findings cannot be shared at this time as the data also forms part of an ongoing study.

References

[1] C.D. Rabadia, Y.J. Liu, L. Wang, H. Sun, L.C. Zhang, Laves phase precipitation in Ti-Zr-Fe-Cr alloys with high strength and large plasticity, Mater. Des. 154 (2018) 228–238, https://doi.org/10.1016/j.matdes.2018.05.035.

[2] A.J. Knowles, A. Bhowmik, S. Purkayastha, N.G. Jones, F. Giuliani, W.J. Clegg, D. Dye, H.J. Stone, Laves phase intermetallic matrix composite in situ toughened by ductile precipitates, Scr. Mater. 140 (2017) 59–62, https://doi.org/10.1016/j.scriptamat.2017.06.043.

[3] Y. Yang, L. Wang, L. Snead, S.J. Zinkle, Development of novel Cu-Cr-Nb-Zr alloys with the aid of computational thermodynamics, Mater. Des. 156 (2018) 370–380, https://doi.org/10.1016/j.matdes.2018.07.003.

[4] S. Huang, X. Zhang, Y. Jiang, Y. Jiang, C. Mao, D. Wu, L. Zhang, L. Liu, Experimental investigation of Ti-Nb-Co ternary system at 1000°C, Mater. Des. 115 (2017) 170–178, https://doi.org/10.1016/j.matdes.2016.11.056.

[5] W. Luo, C. Kirchlechner, X. Fang, S. Brinckmann, G. Dehm, F. Stein, Influence of composition and crystal structure on the fracture toughness of $NbCo_2$ Laves phase studied by micro-cantilever bending tests, Mater. Des. 145 (2018) 116–121, https://doi.org/10.1016/j.matdes.2018.02.045.

[6] J. Huot, E. Akiba, Y. Ishido, Crystal structure of multiphase alloys (Zr, Ti)$(Mn, V)_2$, J. Alloys Compd. 231 (1995) 85–89, https://doi.org/10.1016/0925-8388(95)01842-5.

[7] F. Stein, M. Palm, G. Sauthoff, Structure and stability of Laves phases. Part I. Critical assessment of factors controlling Laves phase stability, Intermetallics 12 (2004) 713–720, https://doi.org/10.1016/j.intermet.2004.02.010.

[8] J. Nei, K. Young, S.O. Salley, K.Y.S. Ng, Determination of C14/C15 phase abundance in Laves phase alloys, Mater. Chem. Phys. 136 (2012) 520–527, https://doi.org/10.1016/j.matchemphys.2012.07.020.

[9] S. Scudino, P. Donnadieu, K.B. Surreddi, K. Nikolowski, M. Stoica, J. Eckert, Microstructure and mechanical properties of Laves phase-reinforced Fe-Zr-Cr alloys, Intermetallics 17 (2009) 532–539, https://doi.org/10.1016/j.intermet.2009.01.007.

[10] L.M. Kang, C. Yang, F. Wang, S.G. Qu, X.Q. Li, W.W. Zhang, Deformation induced precipitation of $MgZn_2$-type laves phase in Ti-Fe-Co alloy, J. Alloys Compd. 778 (2019) 795–802. https://doi.org/10.1016/j.jallcom.2018.11.236.

[11] L.M. Kang, C. Yang, F. Wang, X.X. Li, D.Z. Zhu, W.W. Zhang, W.P. Chen, Y. Huan, Designing ultrafine lamellar eutectic structure in bimodal titanium alloys by semi-solid sintering, J. Alloys Compd. 702 (2017) 51–59, https://doi.org/10.1016/j.jallcom.2017.01.257.

[12] D. Aboudi, S. Lebaili, M. Taouinet, J. Zollinger, Microstructure evolution of diffusion welded 304L/Zircaloy4 with copper interlayer, Mater. Des. 116 (2017) 386–394, https://doi.org/10.1016/j.matdes.2016.12.008.

[13] T. To, F. Célarié, C. Roux-Langlois, A. Bazin, Y. Gueguen, H. Orain, M. Le Fur, V. Burgaud, T. Rouxel, Fracture toughness, fracture energy and slow crack growth of glass as investigated by the Single-Edge Precracked Beam (SEPB) and Chevron-Notched Beam (CNB) methods, Acta Mater. 146 (2018) 1–11, https://doi.org/10.1016/j.actamat.2017.11.056.

[14] U. Ramamurty, S. Jana, Y. Kawamura, K. Chattopadhyay, Hardness and plastic deformation in a bulk metallic glass, Acta Mater. 53 (2005) 705–717, https://doi.org/10.1016/j.actamat.2004.10.023.

[15] R. Bhowmick, R. Raghavan, K. Chattopadhyay, U. Ramamurty, Plastic flow softening in a bulk metallic glass, Acta Mater. 54 (2006) 4221–4228, https://doi.org/10.1016/j.actamat.2006.05.011.

[16] A.E. Giannakopoulos, S. Suresh, Determination of elastoplastic properties by instrumented sharp indentation, Scr. Mater. 40 (1999) 1191–1198, https://doi.org/10.1016/S1359-6462(99)00011-1.

[17] E. Jumaev, S.H. Hong, J.T. Kim, H.J. Park, Y.S. Kim, S.C. Mun, J.-Y. Park, G. Song, J.K. Lee, B.H. Min, T. Lee, K.B. Kim, Chemical evolution-induced strengthening on AlCoCrNi dual-phase high-entropy alloy with high specific strength, J. Alloys Compd. 777 (2019) 828–834, https://doi.org/10.1016/j.jallcom.2018.11.057.

[18] C.D. Rabadia, Y.J. Liu, G.H. Cao, Y.H. Li, C.W. Zhang, T.B. Sercombe, H. Sun, L.C. Zhang, High-strength β stabilized Ti-Nb-Fe-Cr alloys with large plasticity, Mater. Sci. Eng. A 732 (2018) 368–377, https://doi.org/10.1016/j.msea.2018.07.031.

[19] C.D. Rabadia, Y.J. Liu, S.F. Jawed, L. Wang, Y.H. Li, X.H. Zhang, T.B. Sercombe, H. Sun, L.C. Zhang, Improved deformation behavior in Ti-Zr-Fe-Mn alloys comprising the C14 type Laves and β phases, Mater. Des. 160 (2018) 1059–1070, https://doi.org/10.1016/j.matdes.2018.10.049.

[20] F. Stein, G. Sauthoff, M. Palm, Experimental determination of intermetallic phases, phase equilibria, and invariant reaction temperatures in the Fe-Zr system, J. Phase Equilib. 23 (2002) 480, https://doi.org/10.1361/105497102770331172.

[21] V. Raghavan, Fe-Ti-Zr (Iron-Titanium-Zirconium), J. Phase Equilib. 31 (2010) 469, https://doi.org/10.1007/s11669-010-9751-3.

[22] L. Zeng, G. Xu, L. Liu, W. Bai, L. Zhang, Experimental investigation of phase equilibria in the Ti-Fe-Zr system, Calphad 61 (2018) 20–32, https://doi.org/10.1016/j.calphad.2018.02.005.

[23] M.E. Schlesinger, The Mn-Zr (manganese-zirconium) system, J. Phase Equilib. 20 (1999) 79–83, https://doi.org/10.1361/105497199770335983.

[24] V. Ivanchenko, Mn-Ti-Zr (manganese-titanium-zirconium), in: G. Effenberg, S. Ilyenko (Eds.), Non-ferrous Metal Systems. Part 3: Selected Soldering and Brazing Systems, Springer Berlin Heidelberg, Berlin, Heidelberg 2007, pp. 475–485.

[25] Y. Yang, L. Tan, H. Bei, J.T. Busby, Thermodynamic modeling and experimental study of the Fe–Cr–Zr system, J. Nucl. Mater. 441 (2013) 190–202, https://doi.org/10.1016/j.jnucmat.2013.05.061.

[26] L. Wang, L. Xie, Y. Lv, L. Zhang, L. Chen, Q. Meng, J. Qu, D. Zhang, W. Lu, Microstructure evolution and superelastic behavior in Ti-35Nb-2Ta-3Zr alloy processed by friction stir processing, Acta Mater. 131 (2017) 499–510, https://doi.org/10.1016/j.actamat.2017.03.079.

[27] L.C. Zhang, Y. Liu, S. Li, Y. Hao, Additive manufacturing of titanium alloys by electron beam melting: a review, Adv. Eng. Mater. 20 (2018) 1700842, https://doi.org/10.1002/adem.201700842.

[28] L. Zhang, J. Das, H. Lu, C. Duhamel, M. Calin, J. Eckert, High strength Ti–Fe–Sn ultrafine composites with large plasticity, Scr. Mater. 57 (2007) 101–104, https://doi.org/10.1016/j.scriptamat.2007.03.031.

[29] L.C. Zhang, L.Y. Chen, A review on biomedical titanium alloys: recent progress and prospect, Adv. Eng. Mater. 21 (2019) 1801215, https://doi.org/10.1002/adem.201801215.

[30] S.F. Jawed, C.D. Rabadia, Y.J. Liu, L.Q. Wang, Y.H. Li, X.H. Zhang, L.C. Zhang, Mechanical characterization and deformation behavior of β-stabilized Ti-Nb-Sn-Cr alloys, J. Alloys Compd. 792 (2019) 684–693, https://doi.org/10.1016/j.jallcom.2019.04.079.

[31] C. Yang, L.M. Kang, X.X. Li, W.W. Zhang, D.T. Zhang, Z.Q. Fu, Y.Y. Li, L.C. Zhang, E.J. Lavernia, Bimodal titanium alloys with ultrafine lamellar eutectic structure fabricated by semi-solid sintering, Acta Mater. 132 (2017) 491–502, https://doi.org/10.1016/j.actamat.2017.04.062.

[32] L. Zhang, H.-B. Lu, C. Mickel, J. Eckert, Ductile ultrafine-grained Ti-based alloys with high yield strength, Appl. Phys. Lett. 91 (2007) 051906, https://doi.org/10.1063/1.2766861.

[33] H. Zhang, X. Jing, G. Subhash, L.J. Kecskes, R.J. Dowding, Investigation of shear band evolution in amorphous alloys beneath a Vickers indentation, Acta Mater. 53 (2005) 3849–3859, https://doi.org/10.1016/j.actamat.2005.04.036.

[34] L.C. Zhang, J. Xu, Glass-forming ability of melt-spun multicomponent (Ti, Zr, Hf)–(Cu, Ni, Co)–Al alloys with equiatomic substitution, J. Non-Cryst. Solids 347 (2004) 166–172, https://doi.org/10.1016/j.jnoncrysol.2004.09.007.

[35] Y. Zhang, D. Kent, G. Wang, D. St John, M. Dargusch, An investigation of the mechanical behaviour of fine tubes fabricated from a Ti–25Nb–3Mo–3Zr–2Sn alloy, Mater. Des. 85 (2015) 256–265, https://doi.org/10.1016/j.matdes.2015.06.127.

[36] C. Yang, O. Muránsky, H. Zhu, G.J. Thorogood, H. Huang, X. Zhou, On the origin of strengthening mechanisms in Ni-Mo alloys prepared via powder metallurgy, Mater. Des. 113 (2017) 223–231, https://doi.org/10.1016/j.matdes.2016.10.024.

[37] Y.B. Jeong, H.R. Jo, J.T. Kim, S.H. Hong, K.B. Kim, A study on the micro-evolution of mechanical property and microstructures in (Cu-30Fe)-2X alloys with the addition of minor alloying elements, J. Alloys Compd. 786 (2019) 341–345, https://doi.org/10.1016/j.jallcom.2019.01.169.

[38] W. Niu, M.J. Bermingham, P.S. Baburamani, S. Palanisamy, M.S. Dargusch, S. Turk, B. Grigson, P.K. Sharp, The effect of cutting speed and heat treatment on the fatigue life of Grade 5 and Grade 23 Ti–6Al–4V alloys, Mater. Des. 46 (2013) 640–644, https://doi.org/10.1016/j.matdes.2012.10.056.

[39] L. Chen, Q. Zeng, J. Li, J. Lu, Y. Zhang, L.-C. Zhang, X. Qin, W. Lu, L. Zhang, L. Wang, D. Zhang, Effect of microstructure on corrosion behavior of a Zr–Sn–Nb–Fe–Cu–O alloy, Mater. Des. 92 (2016) 888–896, https://doi.org/10.1016/j.matdes.2015.12.067.

[40] P. Qin, Y. Liu, T.B. Sercombe, Y. Li, C. Zhang, C. Cao, H. Sun, L.C. Zhang, Improved corrosion resistance on selective laser melting produced Ti-5Cu alloy after heat treatment, ACS Biomater Sci. Eng. 4 (2018) 2633–2642, https://doi.org/10.1021/acsbiomaterials.8b00319.

[41] L. Chen, J. Li, Y. Zhang, L.-C. Zhang, W. Lu, L. Wang, L. Zhang, D. Zhang, Zr–Sn–Nb–Fe–Si–O alloy for fuel cladding candidate: processing, microstructure, corrosion resistance and tensile behavior, Corros. Sci. 100 (2015) 332–340, https://doi.org/10.1016/j.corsci.2015.08.005.

[42] P. Qin, Y. Chen, Y.-J. Liu, J. Zhang, L.-Y. Chen, Y. Li, X. Zhang, C. Cao, H. Sun, L.-C. Zhang, Resemblance in corrosion behavior of selective laser melted and traditional monolithic β Ti-24Nb-4Zr-8Sn alloy, ACS Biomater Sci. Eng. 5 (2019) 1141–1149, https://doi.org/10.1021/acsbiomaterials.8b01341.

[43] B.D. Beake, A.J. Harris, J. Moghal, D.E.J. Armstrong, Temperature dependence of strain rate sensitivity, indentation size effects and pile-up in polycrystalline tungsten from 25 to 950 °C, Mater. Des. 156 (2018) 278–286, https://doi.org/10.1016/j.matdes.2018.06.063.

[44] Y. Cao, Z. Xue, X. Chen, D. Raabe, Correlation between the flow stress and the nominal indentation hardness of soft metals, Scr. Mater. 59 (2008) 518–521, https://doi.org/10.1016/j.scriptamat.2008.04.039.

[45] A. Ruiz-Moreno, P. Hähner, Indentation size effects of ferritic/martensitic steels: a comparative experimental and modelling study, Mater. Des. 145 (2018) 168–180, https://doi.org/10.1016/j.matdes.2018.02.064.

[46] M.C. Li, M.Q. Jiang, F. Jiang, L. He, J. Sun, Testing effects on hardness of a Zr-based metallic glass under nanoindentation, Scr. Mater. 138 (2017) 120–123, https://doi.org/10.1016/j.scriptamat.2017.05.046.

[47] K.C. Chen, S.M. Allen, J.D. Livingston, Factors affecting the room-temperature mechanical properties of $TiCr_2$-base Laves phase alloys, Mater. Sci. Eng. A 242 (1998) 162–173, https://doi.org/10.1016/S0921-5093(97)00526-1.

[48] Y.J. Liu, S.J. Li, L.C. Zhang, Y.L. Hao, T.B. Sercombe, Early plastic deformation behaviour and energy absorption in porous β-type biomedical titanium produced by selective laser melting, Scr. Mater. 153 (2018) 99–103https://doi.org/10.1016/j.scriptamat.2018.05.010.

[49] M.G. Poletti, G. Fiore, F. Gili, D. Mangherini, L. Battezzati, Development of a new high entropy alloy for wear resistance: FeCoCrNiW0.3 and FeCoCrNiW0.3+5at.% of C, Mater. Des. 115 (2017) 247–254, https://doi.org/10.1016/j.matdes.2016.11.027.

[50] D. Kramer, H. Huang, M. Kriese, J. Robach, J. Nelson, A. Wright, D. Bahr, W.W. Gerberich, Yield strength predictions from the plastic zone around nanocontacts, Acta Mater. 47 (1998) 333–343, https://doi.org/10.1016/S1359-6454(98)00301-2.

[51] S. Xie, E.P. George, Hardness and shear band evolution in bulk metallic glasses after plastic deformation and annealing, Acta Mater. 56 (2008) 5202–5213, https://doi.org/10.1016/j.actamat.2008.07.009.

[52] Z. Yan, K. Wang, Y. Zhou, X. Zhu, R. Xin, Q. Liu, Crystallographic orientation dependent crack nucleation during the compression of a Widmannstätten-structure α/β titanium alloy, Scr. Mater. 156 (2018) 110–114, https://doi.org/10.1016/j.scriptamat.2018.07.023.

[53] L. Lu, Y. Shen, X. Chen, L. Qian, K. Lu, Ultrahigh strength and high electrical conductivity in copper, Science 304 (2004) 422–426, https://doi.org/10.1126/science.1092905.

[54] C.R. Hutchinson, J.F. Nie, S. Gorsse, Modeling the precipitation processes and strengthening mechanisms in a mg-Al-(Zn) AZ91 alloy, Metall. Mater. Trans. A 36 (2005) 2093–2105, https://doi.org/10.1007/s11661-005-0330-x.
[55] J. Wang, M.R.G. Ferdowsi, S.R. Kada, C.R. Hutchinson, M.R. Barnett, Influence of precipitation on yield elongation in Mg-Zn alloys, Scr. Mater. 160 (2019) 5–8, https://doi.org/10.1016/j.scriptamat.2018.09.023.
[56] M. Takeyama, C.T. Liu, Microstructure and mechanical-properties of Laves-phase alloys based on Cr_2Nb, Mater. Sci. Eng. A 132 (1991) 61–66, https://doi.org/10.1016/0921-5093(91)90361-P.
[57] D.D. Risanti, G. Sauthoff, Strengthening of iron aluminide alloys by atomic ordering and Laves phase precipitation for high-temperature applications, Intermetallics 13 (2005) 1313–1321, https://doi.org/10.1016/j.intermet.2004.12.029.
[58] D. Hull, D.J. Bacon, Introduction to Dislocations, fifth ed. Butterworth-Heinemann, Oxford, 2011.
[59] S. Shukla, T. Wang, S. Cotton, R.S. Mishra, Hierarchical microstructure for improved fatigue properties in a eutectic high entropy alloy, Scr. Mater. 156 (2018) 105–109, https://doi.org/10.1016/j.scriptamat.2018.07.022.